Journal of the Optical Society of America A
OPTICS, IMAGE SCIENCE, AND VISION

Automatic classification of atherosclerotic tissue in intravascular optical coherence tomography images

Ping Zhou,* Tongjing Zhu, Chunliu He, and Zhiyong Li

School of Biological Science & Medical Engineering, Southeast University, Nanjing 210096, China
*Corresponding author: capzhou@163.com

Received 13 April 2017; revised 23 May 2017; accepted 26 May 2017; posted 26 May 2017 (Doc. ID 287894); published 21 June 2017

Intravascular optical coherence tomography (IVOCT) has been successfully utilized for *in vivo* diagnostics of coronary plaques. However, classification of atherosclerotic tissues is mainly performed manually by experienced experts, which is time-consuming and subjective. To overcome these limitations, an automatic method of segmentation and classification of IVOCT images is developed in this paper. The method is capable of detecting the plaque contour between the fibrous tissues and other components. Subsequently, the method classifies the tissues based on their texture features described by Fourier transform and discrete wavelet transform. The experimental results of 103 images show that an overall classification accuracy of over 80% in the indicator of depth and span angle is achieved in comparison to manual results. The validation suggests that this method is objective, accurate, and automatic without any manual intervention. The proposed method is able to demonstrate the artery wall morphology successfully, which is valuable for the research of atherosclerotic disease.

OCIS codes: (170.4500) Optical coherence tomography; (170.6935) Tissue characterization; (100.0100) Image processing.

https://doi.org/10.1364/JOSAA.34.001152

1. INTRODUCTION

Coronary artery disease is the leading cause of death in the world [1]. Coronary arteries are the network of arteries that provide the blood supply for the heart. Normally, the vessel wall of the coronary artery is constituted by a layered architecture, comprising intima, media, and adventitia. When the coronary arteries get fatty deposits (plaque) on their inner walls, this condition is called atherosclerosis, which can narrow the arteries and restrict blood flow to the heart. Especially, the rupture of vulnerable atherosclerotic plaques accounts for coronary thrombosis, myocardial ischemia, and sudden cardiac death [2]. Therefore, with the ability to detect plaque vulnerability, a high-resolution imaging technique will advance our understanding of the atherosclerosis process and facilitate the development of therapeutic interventions.

Intravascular optical coherence tomography (IVOCT) [3–5] has drawn the attention of the scientific and clinical communities, with a 10–20 μm resolution and a 0.5–1.5 mm penetration depth. The unique imaging resolution can provide important insights into the physiology of atherosclerosis [6,7]. The image features of atherosclerosis tissues are significant in IVOCT images. Fibrous tissues (FTs) are homogeneous signal-rich regions, and locate close to the lumen and overlay other tissue behind it [8]. Especially, the plaque contour is defined as the border between FT and other tissues in this paper. In addition, lipid tissues (LTs) are signal-poor regions with diffuse borders, and the calcium tissues (CTs) are sharply delineated signal-poor regions with islands of signal-rich regions, and in some cases mixed tissues (MTs) appear as a mixture of both characteristics of CT and LT. Adventitia tissues (ATs) are clearly visualized in segments with slight plaque burden. Therefore, the texture of these tissues presents a unique character that can be used to classify the atherosclerosis tissues [9].

With the goal of automatic tissue discrimination, Xu *et al.* performed quantitative analysis of plaque characterization by the combined parameters of the backscattering coefficient and the attenuation coefficient [10]. Later, van Soest *et al.* demonstrated an algorithm for the automatic quantification of the optical attenuation coefficient [11]. Although these studies have provided a basis for tissue identification in IVOCT images, both approaches were limited due to their parameters, which were analyzed across the entire A-lines without using the characteristics of the plaque region. More recently, growing interest has been raised in exploiting the identification methods based on digital image processing. A semiautomated calcium detection method has been demonstrated by Wang *et al.* combined with edge detection and an active contour model [12]. Based on plaque texture features, random forest (RF) classification methods were proposed by Ughi *et al.* [13] and Athanasiou *et al.* [14]. These works have shown that image-processing techniques can be applied to atherosclerotic classification, which can significantly improve the accuracy of IVOCT images automatic analysis.

In this paper, we propose an automatic method for segmentation and classification of atherosclerosis composition based on image-processing techniques. To make full use of the characteristics of the plaque region, the plaque contour is proposed for the first time. Due to the same properties of the pixels behind the plaque contour, the FT, CT, and AT can be classified easily. Subsequently, the residual pixels can be divided into two categories by the RF classifier. Compared with recently published works, only a small part of the pixels of the OCT image needs be processed in our algorithm, so that it greatly improves efficiency and reduces the complexity of the classifier. The proposed approach is validated against manual assessments by experienced readers.

2. MATERIALS AND METHODS

A. OCT Images

The coronary IVOCT imaging study was performed at Nanjing Drum Tower Hospital. This study was approved by the internal review board and informed written consent was obtained. The OCT system is a C7-XR Fourier-domain OCT system (Lightlab Inc., Westford, Massachusetts, U.S.) by using the C7 Dragonfly catheter. It provides an axial resolution of 15 μm and a lateral resolution of 19 μm. Each frame consists of 504 lines × 976 pixels, resulting in 5.12 μm per pixel. After conversion by bilinear interpolation, the size of corresponding Cartesian image is 1953 pixels × 1953 pixels. In this study, 10 OCT pullbacks from nine patients were used to validate the proposed methodology.

B. Methodology Pipeline

The entire plaque analysis method is implemented based on the plaque contour and the texture features, as shown in Fig. 1. First, after the segmentation of the lumen and the tissue area, the catheter, the guide wire, and the lumen contour are detected. Then, the plaque contour is localized by bilateral filter, gradient operator, and threshold method. Finally, segmentation of CT is achieved by a level set algorithm. Classification of AT, LT, and MT is implemented by texture analysis methods, including spectral description and statistics matrix.

C. Detection of Lumen Contour

The Otsu's threshold [15] is performed in the polar IVOCT image [Fig. 2(a)], and this identifies three large structures: the catheter artifact, the guide wire, and the arterial wall. The catheter artifact is removed by Hough transformation, and the guide wire by an area constrain. The first nonzero pixels of arterial wall are detected based on scanning each A-line from top to bottom [Fig. 2(b)]. Subsequently, these pixels are connected using cubic interpolation, and the result is converted into Cartesian coordinates to generate an initial lumen contour [Fig. 2(c)]. Finally, the contour is evolved based on the active contour model [16] to detect lumen accurately [Fig. 2(d)]. The signal out of the limited penetration of IVOCT has a sharply decreased signal-to-noise ratio. The outer boundary (OB) is the maximum penetration depth of IVOCT, locating at a penetration of 1.5 mm [14]

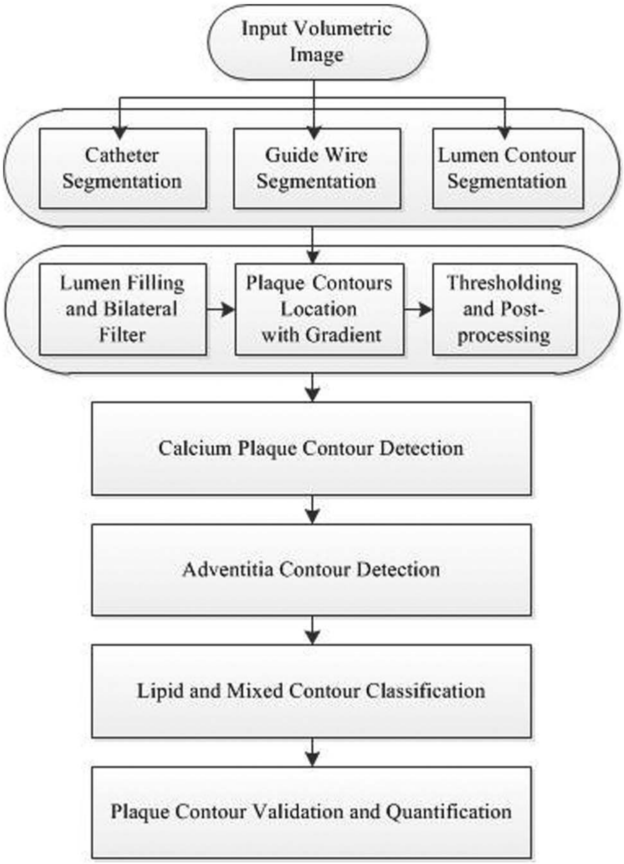

Fig. 1. Flow chart of the entire method.

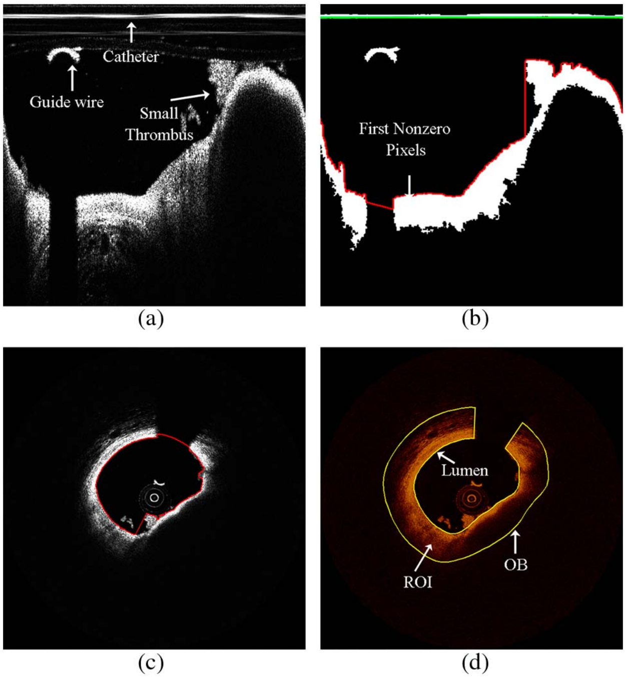

Fig. 2. Detection of lumen contour and ROI. (a) Original polar image; (b) connecting of first nonzero pixels; (c) initial lumen contour in Cartesian image; and (d) ROI.

in the light-propagation. Therefore, only the area enclosed by lumen contour and OB is considered in this paper, which is the defined region of interest (ROI) [Fig. 2(d)].

D. Detection of the Plaque Contour

The border of CT and AT is sharp, and the difference of signal intensity of the FT and LT region is significant; therefore, detection of the plaque contour can be implemented by the edge detection method. However, due to the blur and noise of the border, image preprocessing should be performed first by sequential approaches. The Cartesian IVOCT image is transformed into a parameter image by log operator and normalization processing. The lumen contour is filled with the average value of superficial vessel wall to exclude the lumen in the following detection steps. A bilateral filter is implemented to enhance border information and to reduce noise.

After image preprocessing, the searching region covering the tissue border is detected by the derivative operator of a Gauss filter due to its two salient features. The Gauss part of the operator reduces the intensity of structures, including noise at scales much smaller than the standard deviation σ. Here, the preprocessed image is denoted as $I_p(x, y)$, and the Gaussian function is denoted as $G(x, y)$

$$G(x, y) = \exp\left(-\frac{x^2 + y^2}{2\sigma^2}\right), \tag{1}$$

$$I_s(x, y) = G(x, y) \otimes I_p(x, y). \tag{2}$$

The derivative part of the operator is sensitive to gradient information at the tissue border. The gradient magnitude $M(x, y)$, also referred as the gradient image [Fig. 3(a)], is obtained from

$$I_x = \frac{\partial}{\partial x} I_s = \frac{-x}{4\pi\sigma^4} \exp\left(-\frac{x^2 + y^2}{2\sigma^2}\right) \otimes I_p(x, y), \tag{3}$$

$$I_y = \frac{\partial}{\partial y} I_s = \frac{-y}{4\pi\sigma^4} \exp\left(-\frac{x^2 + y^2}{2\sigma^2}\right) \otimes I_p(x, y), \tag{4}$$

$$M(x, y) = \sqrt{I_x^2 + I_y^2}. \tag{5}$$

The plaque contour detection is performed in the gradient image; this includes the following steps. The areas out of OB and behind the guide wire are removed to exclude ineffective information [Fig. 3(b)], and then a binary image is automatically obtained by the hysteresis threshold [17] method [Fig. 3(c)]. Subsequently, the border-searching region in the binary image is automatically recognized by applying an area threshold (Th_Area). However, some connected components adjoining lumen contour are improper, which are generated by inaccurate lumen detection. The average distance from each pixel of the components to lumen is used to delete improper components by a cutoff value (Th_Dist) [Fig. 3(d)]. The plaque contour is finally obtained by calculating the skeleton line of each of the remaining connected components [Fig. 3(e)].

E. Classification of CTs and ATs

Calcium plaque with a sharp border is the easiest to be detected; it has been studied by many research groups. According to the proposed methods, the calcium plaque contour is initialized by K-means algorithm [14] and then evolved using a level-set model [12].

Adventitia is represented as layer structural textures that go along the tangential direction. With the advantage of describing the directionality of periodic patterns, the spectral approach is ideally suitable for AT classification.

Adventitia detection based on the plaque contour and spectral approach is illustrated in Fig. 4. The three lines in the top left of the figure from the inside to the outside are the plaque contour, middle line, and OB. The middle line is defined as the middle position between the plaque contour and OB in the

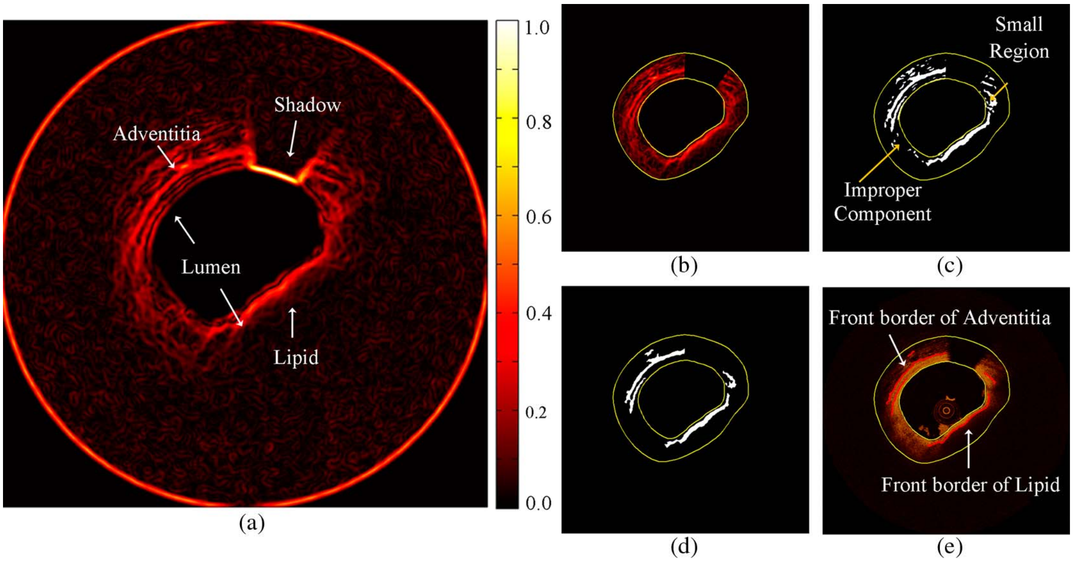

Fig. 3. Location of the plaque contour. (a) Gradient image; (b) remove the areas out of OB and behind the guide wire; (c) binary image through hysteresis threshold; (d) remove improper components and small regions; (e) location results of the plaque contour.

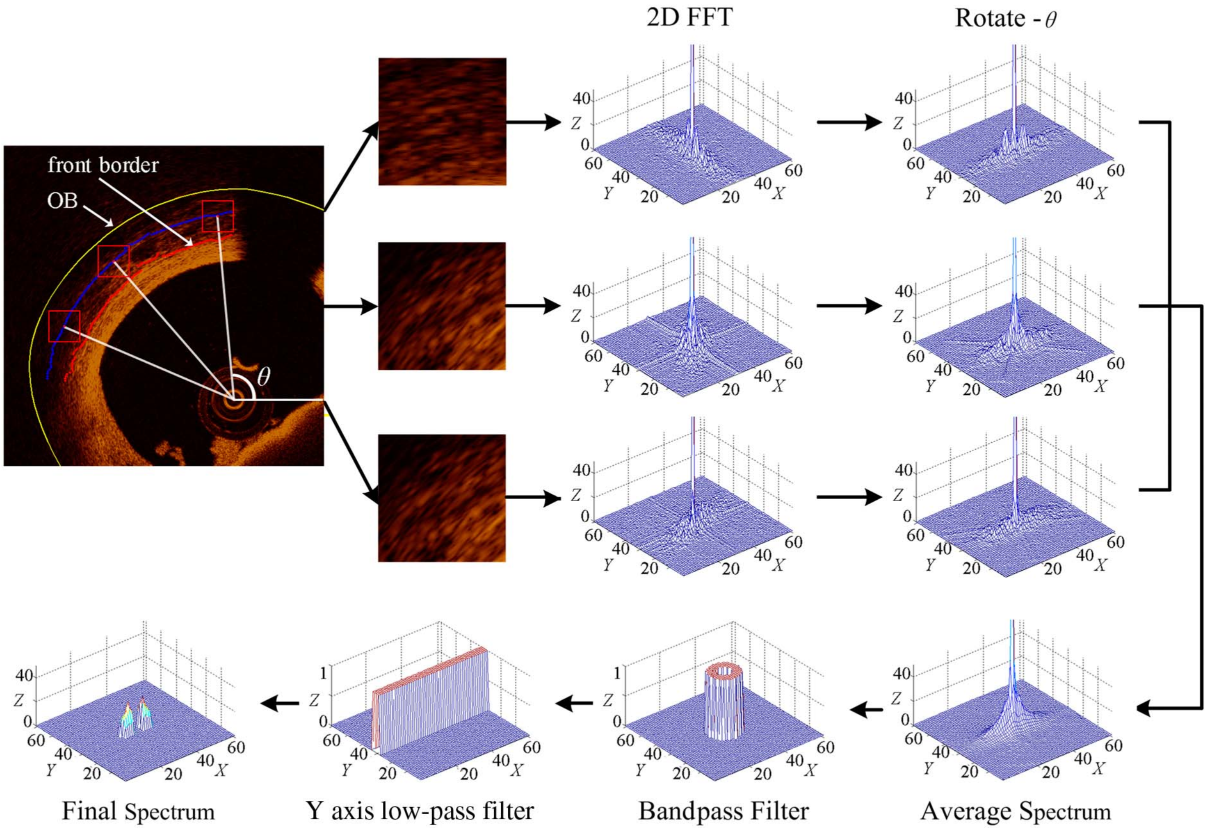

Fig. 4. Adventitia detection based on the plaque contour and spectral approach.

radial direction. For the ith pixel in the middle line, the rotate angle θ_i is calculated and a 64 pixel × 64 pixel neighborhood is selected (shown as red box in top left of Fig. 4). It is obvious that the 2D fast Fourier transform (FFT) spectrum of the neighborhood is sensitive to the rotate angle θ_i due to the directional property of layer structural texture. Therefore, the spectrum is rotated $-\theta_i$ to align spectral energy in the same direction along the x axis. Subsequently, all the rotated spectra are used to calculate the average spectrum to reduce the impact of noise. Due to the fundamental spatial period of the texture patterns, the average spectrum is passed by a bandpass filter, where D_{BP} is the radial center of the band and W is the width of the band. Eventually, the final spectrum is obtained by a y axis low-pass filter, where D_{LP} is the cutoff frequency.

The final spectrum contains enough information to classify the adventitia border. For the same kind of tissue, the total energy of the final spectrum is stable. For different kinds of tissue, the total energy of the final spectrum is significantly different. Therefore, classification of AT is performed simply by comparing the accumulation sum of the final spectrum with the presetting threshold *Th_Adven*.

F. Classification of LTs and MTs

Considering the properties of lipid and mixed plaque, texture feature vectors based on discrete wavelet transformation (DWT) [18] is defined to characterize the geometric feature of these two tissues. First, the tissue regions of lipid and mixed plaques between the plaque contour and OB are obtained, which is defined as classification regions. As shown in Fig. 5(a), for each pixel of classification regions, a 64 pixel × 64 pixel neighborhood is denoted as the local image I_0. The first-level DWT decomposition of I_0 using the Daubechies basis generates four components, including one low-pass subimage I^1_{LL} and three high-pass subimages I^1_{LH}, I^1_{HL}, I^1_{HH}. The low-pass subimage I^1_{LL} can be further decomposed, generating the second-level DWT decomposition components I^2_{LL}, I^2_{LH}, I^2_{HL}, I^2_{HH}. Here, I^1_{LL} presents the principal geometric feature of local image I_0, and I^k_{LH} and I^k_{HL} $(k = 1, 2)$ present most high-pass information for each level of resolution along the two coordinate axes x and y. To make the feature vector insensitive to rotation, I_{LH} and I_{HL} at each level are processed as

$$I_k(i,j) = \sqrt{|I^k_{\mathrm{LH}}(i,j)|^2 + |I^k_{\mathrm{HL}}(i,j)|^2}. \tag{6}$$

Finally, the I^1_{LL} and I_k $(k = 1, 2)$ are selected as the feature subimage group.

The texture feature vectors are obtained by the following steps for each feature subimage. For example, the means $u(n)$ and the variances $\sigma(n)$ of I^1_{LL} within nth different spherical shells are calculated [shown in Fig. 5(b)], where n is the index. Specifically, the inner radius of spherical shells is $(n-1)\Delta r$, and the outer radius is $n\Delta r$, where Δr is the constant thickness of spherical shells. Subsequently, a relatively short vector V_{LL} of I^1_{LL} can be obtained as

$$V_{\mathrm{LL}} = [u(1), u(2), \ldots, u(N), \lambda\sigma(1), \lambda\sigma(2), \ldots, \lambda\sigma(N)], \tag{7}$$

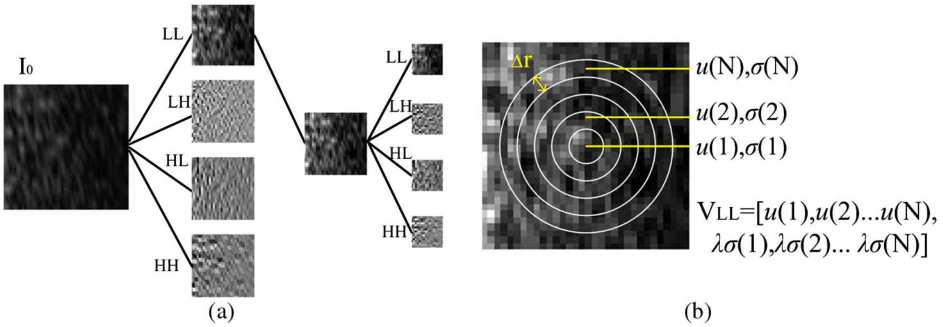

Fig. 5. (a) Wavelet decomposition subimages; (b) structure of the feature vector.

where the λ is the weight. Finally, the short vector V_1 and V_2 are calculated, and the feature vectors are represented as $V = [V_{\mathrm{LL}}, V_1, V_2]$.

The previous feature vector of the pixels belonging to classification regions are used as the input of the RF algorithm [19]. First, the RF classifier is trained by a training set. Then the pixels are classified into two classes: LT and MT. As mentioned earlier, the classification regions behind plaque contour are always composed of only one kind of plaque tissue; therefore, the classification task is performed by the proportion of pixels classes.

3. RESULTS

A. Computing Time of the Algorithms

All algorithms are implemented on a personal computer (I3 CPU at 3.30 GHz, 2G memory) in MATLAB R2012b. The computing time for plaque contour segmentation is ~2.2 s. The time required by AT detection is ~1.6 s. Based on plaque contour, the number of pixels to be classified accounts for 35 ± 17% of the pixels in the original ROI. The time for computing texture feature vector based on wavelet decomposition requires ~10.9 s, while the RF classification takes ~1.7 s.

B. Result of Lumen Detection

We randomly selected 217 IVOCT images from the data set of 10 OCT pullbacks, the lumen contour of which is manually marked by an experienced reader. Specially, the proposed method in this paper was suitable for plaque images without stents and big thrombus. The lumen detection is shown in Fig. 6.

In order to validate the efficiency of the method, the expert's manual analysis results and the automatic analysis results were compared in the indicator of lumen area. The Pearson correlation coefficient was calculated, and Bland–Altman analysis was performed. As shown in Fig. 7, there was a consistency between the manual and automatic results, with a high linear correlation of 0.99, low average error of 0.09, and low standard deviation of 0.09.

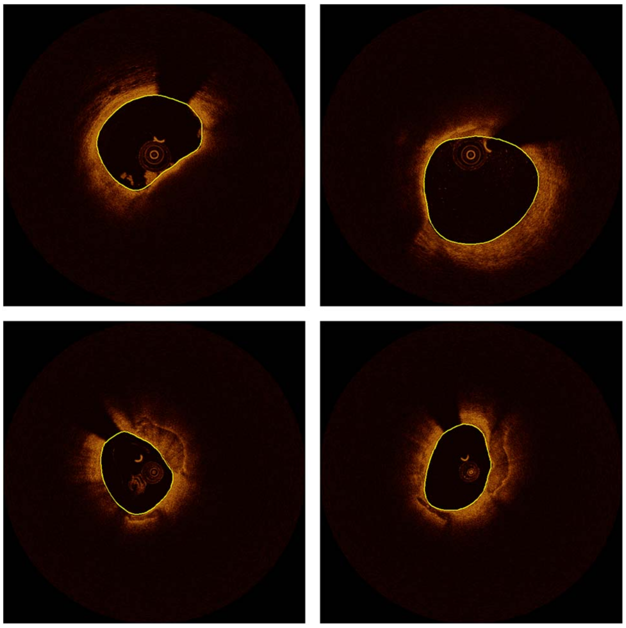

Fig. 6. Results of lumen detection.

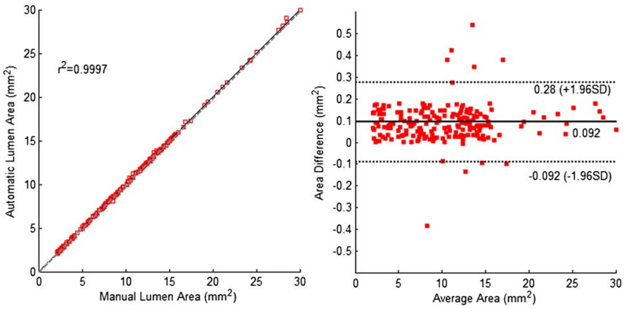

(a) (b)

Fig. 7. (a) Correlation plot and (b) Bland–Altman plots for lumen areas.

Table 1. Optimal Parameters for the Algorithms

Parameter	Value
σ	8
Th_Area	500 pixels
Th_Dist	19 pixels
D_{BP}	$6/64 * 2$ pi
W	$2/64 * 2$ pi
D_{LP}	$2/64 * 2$ pi
Th_Adven	390 intensity

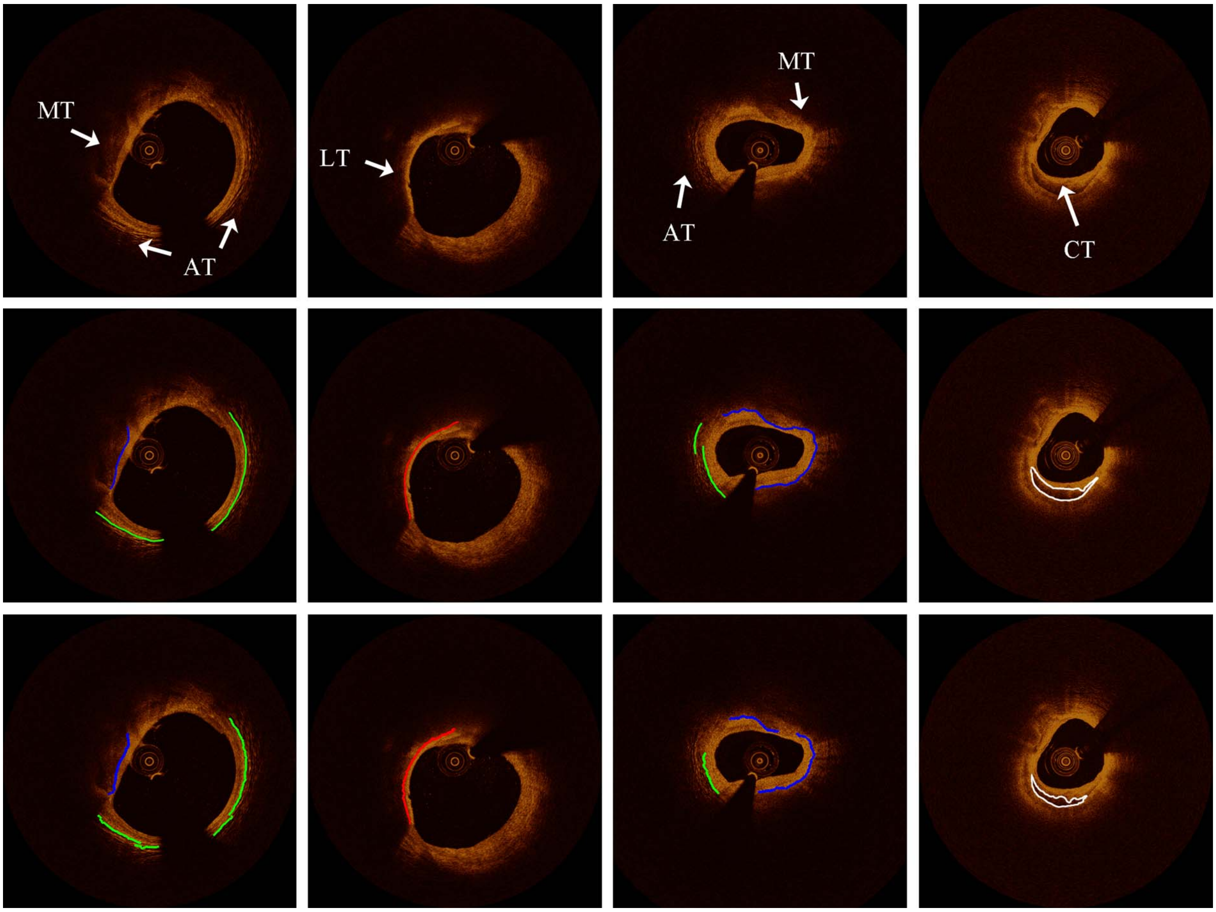

Fig. 8. Results of tissue classification. The colors of the plaque contour indicate the tissue behind the border (green, AT; red, LT; blue, MT; and white, CT.

C. Result of Tissue Classification

To verify the performance of the tissue classification method, 103 images were selected by two experts. The features of these images, including obvious morphology, facilitate the classification task. 281 tissue regions including 54 calcium plaques, 75 ATs, 48 lipid plaques, and 104 mixed plaques were marked. Then the two manual results were processed by the average method, and the mean estimation was used as the gold standard.

All these selected images were used for optimal tuning of the algorithm parameters. Optimal parameters for the algorithms had been determined based on visual inspection of the results. The final parameters are shown in Table 1.

The training set of RF was created by randomly selecting 60 of the total 152 lipid and mixed plaques. After parameter tuning by this training set, the specific set with 100 trees and eight variables were selected as the required parameters. The remaining 92 plaques were used as the testing set. A number of $\sim 2.4 \cdot 10^5$ training pixels were analyzed, resulting in a total of $\sim 1.6 \cdot 10^6$ testing pixels. The pixel-wise classification accuracy of 91.5% for lipid plaques and 78.1% for mixed plaques was found.

The performance of the entire analysis method is validated based on the accuracy of the plaque contour detection. Figure 8 shows examples of the automated classification results (lowest row) for adventitia, lipid, mixed and calcium plaque, respectively, as well as manual classification (middle row). For calcium plaque, the boundaries are well detected by level set method. For AT, the plaque contour is discontinuous because

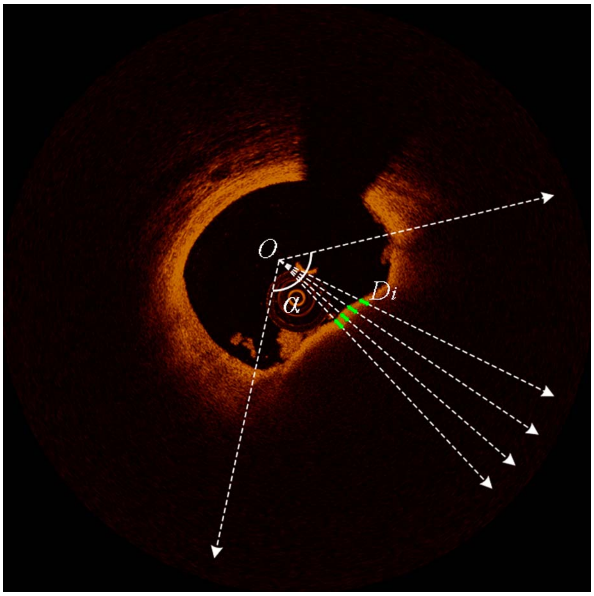

Fig. 9. Quantification metrics.

Table 2. Mean ± Standard Deviation of Quantitative Measurement Differences

		Cal	Adventitia	Liq	Mix
Depth	Absolute	0.03 ± 0.03 mm	0.04 ± 0.07 mm	0.04 ± 0.05 mm	0.09 ± 0.11 mm
	Relative	$16.1 \pm 16.1\%$	$7.1 \pm 12.8\%$	$19.2 \pm 23.6\%$	$17.8 \pm 21.7\%$
AFF	Absolute	6.6 ± 9.4 deg	35.5 ± 30.6 deg	8.6 ± 11.8 deg	15.3 ± 10.8 deg
	Relative	$10.4 \pm 14.9\%$	$33.8 \pm 29.1\%$	$14.4 \pm 19.8\%$	$18.9 \pm 13.5\%$

of the process of threshold of gradient image and removal of small connected components. For lipid plaque, the sensitivity of the plaque contour location algorithm has good performance due to the obvious difference of intensity. For mixed plaque, the plaque contour is accurately detected but discontinuous in some cases, which has a slight effect on the performance of the proposed method.

Two quantitative indicators, depth and span angle, were calculated automatically for each plaque-contour, as shown in Fig. 9. With the reference of the centroid, the depth was defined as

$$\text{Depth} = \frac{1}{n}\sum_{i=1}^{n} D_i,$$

where n is the pixel number of the tissue border. The span angle α (indicated by AFF) was denoted as the largest angle between the rays across the plaque region.

The quantitative validation of depth and AFF showed excellent agreement. The absolute and relative differences between the automatic and manual method are given in Table 2. Overall, the accuracy of >80% in the indicator of depth for all types of tissue suggested reasonable agreement between the automatic and manual results. Also, accuracy >80% in the indicator of AFF was achieved for all types of tissue except for AT, which results in a low accuracy of 66.2%.

4. DISCUSSION

Plaque morphology has played a more and more important role in the study of cardiovascular disease. The morphology is defined as the composition of artery wall and geometric shape of atherosclerotic plaques. Based on this information, the mathematical model of cardiovascular hemodynamics is important to advance the general understanding of coronary atherosclerotic disease and facilitate the development of new therapies and interventions. A few papers have been published recently that made mention of detecting plaque morphology. The parametric techniques focused on the signal across the A-line and detected the division points of different layers. However, there was no association among these division points.

For what we believe is the first time, a detection method of the plaque contour based on image processing is proposed. The plaque contour is defined as the border between fibrous and other tissues, which can demonstrate plaque morphology successfully. Therefore, this is a complete framework for all atherosclerotic tissues without any manual interaction. The good agreement between the automatic and experts' manual results confirms the effectiveness of this method (CT:0.03 ± 0.03 mm, AT:0.04 ± 0.07 mm, LT:0.04 ± 0.05 mm).

The proposed method is capable of detecting the plaque structure of clinical significance such as the thin-cap fibroatheroma (TCFA) and lipid core. In addition, the method has the advantages of high accuracy and provides objective and robust analysis results, avoiding the manual factors in the process. Therefore, the promotion of this method is significant enough to be integrated in clinical routines, which contributes to the diagnosis and treatment of atherosclerotic disease. As an example, characterization and quantification of the atherosclerotic tissues can be valuable both for preprocedure and postprocedure observation of percutaneous coronary intervention (PCI).

A limitation of the proposed method is the fact that the plaque contour location results are discontinuous, especially in the adventitia region, which decreases detection sensitivity and accuracy. In addition, validation is performed using experts' manual analysis as the gold standard in this paper. However, except for calcium plaque with sharply boundaries and AT with lamellar texture, most LTs and MTs were not typical, so that it is difficult for experts to derive reliable assessments. Therefore, the histological data or intravascular ultrasound (IVUS) images are required as additional information, the purpose of which is to give more objective and detailed analysis.

There is still significant work required to improve accuracy and extend the application. IVOCT images are intrinsically three-dimensional; therefore, three-dimensional methods are more robust and efficient to implement segmentation, detection, and classification tasks. In addition, automated detection of coronary stent struts in IVOCT images is of importance. Further development of the methodology includes improving tissue border location performance to reduce the sensitivity to the shadow behind stents.

5. CONCLUSION

We presented an automatic analysis method for arteriosclerosis tissues through IVOCT images. The innovative aspects of the proposed method are: (1) automatic analysis without any manual intervention; (2) the plaque contour defined in this paper plays a key role in accurate segmentation of arteriosclerosis tissues; (3) detection of adventitia and LTs relied on the spectral approach. The validation shows that this method is objective and accurate, which is valuable for the diagnosis and treatment of atherosclerotic disease.

Funding. National 973 Basic Research Program of China (2013CB733800); National Natural Science Foundation of China (NSFC) (11272091, 11422222, 11572087, 31470043); Australian Research Council (ARC) (FT140101152).

REFERENCES

1. W. S. Weintraub, S. R. Daniels, L. E. Burke, B. A. Franklin, G. C. Goff, L. L. Hayman, D. Lloydjones, D. K. Pandey, E. J. Sanchez, and A. P. Schram, "Value of primordial and primary prevention for cardiovascular

disease: a policy statement from the American Heart Association," Circulation **124**, 967–990 (2011).

2. S. C. Smithjr, A. Collins, R. Ferrari, D. R. Holmesjr, S. Logstrup, D. Vacamcghie, J. Ralston, R. L. Sacco, H. Stam, and K. Taubert, "Our time: a call to save preventable death from cardiovascular disease (heart disease and stroke)," Eur. Heart J. **60**, 2343–2348 (2012).
3. J. E. Phipps, T. Hoyt, T. E. Milner, and M. D. Feldman, "Translating intravascular optical coherence tomography from a research to a clinical tool," Curr. Cardiovasc. Imaging Rep. **8**, 1–8 (2015).
4. I. K. Jang, B. E. Bouma, D. H. Kang, S. J. Park, S. W. Park, K. B. Seung, K. B. Choi, M. Shishkov, K. Schlendorf, and E. Pomerantsev, "Visualization of coronary atherosclerotic plaques in patients using optical coherence tomography: comparison with intravascular ultrasound," J. Am. Coll. Cardiol. **39**, 604–609 (2002).
5. L. S. Athanasiou, N. Bruining, F. Prati, and D. Koutsouris, "Optical coherence tomography: basic principles of image acquisition," in *Intravascular Imaging: Current Applications and Research Development*, V. D. Tsakanikas, ed. (Medical Information Science Reference, 2012), pp. 306–307.
6. T. Kubo, T. Imanishi, S. Takarada, A. Kuroi, S. Ueno, T. Yamano, T. Tanimoto, Y. Matsuo, T. Masho, and H. Kitabata, "Assessment of culprit lesion morphology in acute myocardial infarction: ability of optical coherence tomography compared with intravascular ultrasound and coronary angioscopy," J. Am. Coll. Cardiol. **50**, 933–939 (2007).
7. R. Huber, D. C. Adler, and J. G. Fujimoto, "Buffered Fourier domain mode locking: unidirectional swept laser sources for optical coherence tomography imaging at 370, 000 lines/s," Opt. Lett. **31**, 2975–2977 (2006).
8. H. Yabushita, B. E. Bouma, S. L. Houser, H. T. Aretz, I. K. Jang, K. H. Schlendorf, C. R. Kauffman, M. Shishkov, D. H. Kang, and E. F. Halpern, "Characterization of human atherosclerosis by optical coherence tomography," Circulation **106**, 1640–1645 (2002).
9. I. K. Jang, G. J. Tearney, B. Macneill, M. Takano, F. Moselewski, N. Iftima, M. Shishkov, S. Houser, H. T. Aretz, and E. F. Halpern, "In vivo characterization of coronary atherosclerotic plaque by use of optical coherence tomography," Circulation **111**, 1551–1555 (2005).
10. C. Xu, J. M. Schmitt, S. G. Carlier, and R. Virmani, "Characterization of atherosclerosis plaques by measuring both backscattering and attenuation coefficients in optical coherence tomography," J. Biomed. Opt. **13**, 034003 (2008).
11. G. Van Soest, T. Goderie, E. Regar, S. Koljenović, G. L. van Leenders, N. Gonzalo, N. S. Van, T. Okamura, B. E. Bouma, and G. J. Tearney, "Atherosclerotic tissue characterization in vivo by optical coherence tomography attenuation imaging," J. Biomed. Opt. **15**, 011105 (2010).
12. Z. Wang, H. Kyono, H. G. Bezerra, H. Wang, M. Gargesha, C. Alraies, C. Xu, J. M. Schmitt, D. L. Wilson, and M. A. Costa, "Semiautomatic segmentation and quantification of calcified plaques in intracoronary optical coherence tomography images," J. Biomed. Opt. **15**, 061711 (2010).
13. G. J. Ughi, A. Tom, S. Peter, D. Walter, and D. H. Jan, "Automated tissue characterization of in vivo atherosclerotic plaques by intravascular optical coherence tomography images," Biomed. Opt. Express **4**, 001014 (2013).
14. L. S. Athanasiou, C. V. Bourantas, G. Rigas, A. I. Sakellarios, T. P. Exarchos, P. K. Siogkas, A. Ricciardi, K. K. Naka, M. I. Papafaklis, and L. K. Michalis, "Methodology for fully automated segmentation and plaque characterization in intracoronary optical coherence tomography images," J. Biomed. Opt. **19**, 026009 (2014).
15. X. Xu, S. Xu, L. Jin, and E. Song, "Characteristic analysis of Otsu threshold and its applications," Pattern Recognit. Lett. **32**, 956–961 (2011).
16. M. Kass, A. Witkin, and D. Terzopoulos, "Snakes: active contour models," Int. J. Comput. Vis. **1**, 321–331 (1988).
17. R. Medina-Carnicer, A. Carmona-Poyato, R. Muñoz-Salinas, and F. J. Madrid-Cuevas, "Determining hysteresis thresholds for edge detection by combining the advantages and disadvantages of thresholding methods," IEEE Trans. Image Process. **19**, 165–173 (2010).
18. Z. Xue, D. Shen, and C. Davatzikos, "Determining correspondence in 3-D MR brain images using attribute vectors as morphological signatures of voxels," IEEE Trans. Med. Imaging **23**, 1276–1291 (2004).
19. A. L. Boulesteix, S. Janitza, J. Kruppa, and I. R. König, "Overview of random forest methodology and practical guidance with emphasis on computational biology and bioinformatics," Wiley Interdiscip. Rev. **2**, 493–507 (2012).